ARGONNE NATIONAL LABORATORY
9700 South Cass Avenue
Argonne, IL 60439

ANL/MCS-TM-211

The Structure of a Moving Vortex Lattice

by

D. W. Braun, G. W. Crabtree,* H. G. Kaper, A. E. Koshelev,†
G. K. Leaf, D. M. Levine, and V. M. Vinokur*

Mathematics and Computer Science Division

Technical Memorandum No. 211

November 1995

This work was supported by the Mathematical, Information, and Computational Sciences Division subprogram of the Office of Computational and Technology Research and the Materials Sciences Office of the U.S. Department of Basic Energy Sciences Program under Contract No. W-31-109-Eng-38, and by the National Science Foundation Office of the Science and Technology Center, under Contract No. DMR-91-20000.

*Materials Science Division, Argonne National Laboratory

†Also: Institute of Solid State Physics, Chernogolovka, Moscow District, 142432, Russia

Contents

The Structure of a Moving Vortex Lattice

D. W. Braun, G. W. Crabtree, H. G. Kaper, A. E. Koshelev,
G. K. Leaf, D. M. Levine, V. M. Vinokur

Abstract

Numerical solutions of the time-dependent Ginzburg-Landau equations show a new mechanism for plastic motion of a driven vortex lattice in a clean superconductor. The mechanism, which involves the creation of a defect superstructure, is intrinsic to the moving vortex lattice and is independent of bulk pinning. Other structural features found in the solutions include a reorientation of the vortex lattice and a gradual healing of lattice defects under the influence of a transport current.

1. Introduction and Outline of Results

Recently, attention has focused increasingly on the dynamic states of a vortex system. Much of the interest concerns the type of motion of a vortex lattice under an applied current [1–3]. It has been observed that, in a significant region of the phase diagram below the vortex lattice melting line, vortex motion is predominantly plastic motion. The explanation given in [1,2] relies heavily on the notion that the vortex interactions compete with a randomness in the driven vortex system [4,5]. In this note, we present the results of a numerical study of the motion of a vortex lattice in a clean finite sample and find a different mechanism for plastic vortex motion. Past considerations excluded the effects of the current-induced magnetic field. We show that a current increases the vortex spacing in the direction of vortex motion and enforces the formation of *fault lines* to accommodate the resulting strains. The fault lines serve as a source of plastic deformations. The mechanism is the result of the intrinsic behavior of the vortex lattice and is independent of bulk pinning. It may be responsible for plastic motion in very clean superconductors.

The structure of a vortex lattice moving under the influence of a transport current in a homogeneous superconducting sample depends on the relative strengths of the Lorentz force and the barrier forces associated with the free surfaces [6]. Numerical solutions of the time-dependent Ginzburg-Landau (TDGL) equations [7] show that the barrier forces dominate at weak currents. Vortex motion is confined to the interior of the sample, and the vortex lattice is essentially static. Its close-packed rows align with the free surfaces. The lattice structure may have defects, whose origin can be traced to the transient phase, but these defects disappear gradually, and a more or less uniform structure with isolated defects remains. When the Lorentz force dominates, vortices enter and leave through the free surfaces, and the entire vortex lattice moves steadily across the sample. The lattice structure changes in two ways. We see a change in the orientation of the lattice, where

the close-packed rows align with the direction of the Lorentz force, and the development of a defect superstructure, where one or several distinct "fault lines" separate regions of approximately uniform structure. A fault line consists of several aligned dislocations and finite segments of a 30° boundary. The fault lines remain more or less stationary as the lattice moves. They provide the principal mechanism supporting the gradient of the vortex density induced by the self-field of the current and serve as a source of plastic deformations. Similar defect structures have been observed in decorations of static vortex lattices with density gradients [8,9].

2. The Ginzburg-Landau Model of Superconductivity

The TDGL model of superconductivity consists of an evolution equation for the complex order parameter ψ, an expression for the supercurrent density $\mathbf{j}_s$, and Ampère's law, which connects the supercurrent density to the vector potential $\mathbf{A}$,

$$\left(\frac{\partial}{\partial t} + i\kappa\phi\right)\psi = -\left(\frac{\nabla}{i\kappa} - \mathbf{A}\right)^2 \psi + \left(1 - |\psi|^2\right)\psi, \tag{1}$$

$$\mathbf{j}_s = \frac{1}{2i\kappa}(\psi^*\nabla\psi - \psi\nabla\psi^*) - |\psi|^2\mathbf{A}, \tag{2}$$

$$\sigma\left(\frac{\partial \mathbf{A}}{\partial t} + \nabla\phi\right) = -\nabla\times\nabla\times\mathbf{A} + \mathbf{j}_s. \tag{3}$$

Equations (1)–(3) are dimensionless: Lengths are measured in units of the penetration depth λ; time in units of ξ^2/D (ξ the coherence length, D the normal diffusion coefficient); fields in units of $H_c\sqrt{2}$ (H_c the thermodynamic critical field); and current densities in units of $(cH_c\sqrt{2})/(4\pi\lambda)$. The order parameter is normalized so $\psi = 1$ at equilibrium in the absence of fields. At a free surface, $\mathbf{j}_s \cdot \mathbf{n} = 0$.

Adopting the zero-electric potential gauge, we enforce the identity $\phi = 0$ at all times. We maintain gauge invariance by computing the link variables instead of the vector potential. Details of the numerical procedure are described in [10]. In all computations reported here, the Ginzburg-Landau parameter $\kappa = 4$ and the normal conductivity $\sigma = 1$. In our system of dimensionless variables, $H_{c1} = (\ln\kappa + 0.5)/(2\kappa) = 0.24$, $H_c = 1/\sqrt{2} = 0.71$, and $H_{c2} = \kappa = 4$. The BCS depairing-current density is $j_{\rm BCS} = (2\sqrt{3}/9)$; see [11, Eq. (4-36)].

The computations were done for a homogeneous pin-free superconducting sample, infinite in the z direction, periodic in the y direction, and bounded in the x direction. The magnetic field is in the positive z direction, and any transport current is in the positive y direction. Thus, the only variations occur in the (x, y) plane, and any Lorentz force acts in the positive x direction. The free surfaces are along the left and right edges of the sample. A transport current J in the positive y direction is induced by a field differential between the left and right surface: $H_l = H_0 + \Delta H$, $H_r = H_0 - \Delta H$, where $\Delta H = \frac{1}{2}J$.

3. Configuration and Procedural Details

Unless otherwise noted, all results refer to a standard configuration, whose cross section in the (x, y) plane measures 32×48 (units of λ). Our standard choice for the applied magnetic field is $H_0 = 0.8$ ($H_0 \approx 1.13 H_c$ in dimensional terms), with $\Delta H = 0$ (no current), $\Delta H = 0.125$ ("weak" current), $\Delta H = 0.250$ ("intermediate" current), or $\Delta H = 0.500$ ("strong" current). The corresponding current densities are approximately 0, 2, 4, and 8% of the BCS depairing-current density.

The numerical algorithm uses a one-step forward Euler time integration technique; the (dimensionless) time step is 0.0025 units of time. Starting from the Meissner state, established at $H_0 = 0.01$, we increase the strength of the applied field to $H_0 = 0.8$, apply the transport current as appropriate, and let the system evolve through the transient phase. As a working definition, we assume that the steady state is reached when the time variation in the total number of vortices in the sample is less than 1% over 200 units of time (80,000 time steps). The average number of vortices in the steady state varies from 230 (no current) to 660 (strong current). The steady state is usually well established after about 4,500 units of time (1.8 million time steps). Only at that time do we begin to record data, normally at intervals of 10 units of time (4,000 time steps), for approximately 1,500 units of time (600,000 time steps). The recorded data are stored for postprocessing.

In the postprocessing phase, we first compute the magnetic induction as a function of x (along the Lorentz force), taking averages in the y direction (along the current). For each recorded time step, we then determine the position of every vortex in the sample from the order parameter and assemble these positions into vortex trajectories. The trajectories indicate the nature of the vortex motion. The structure and evolution of the vortex lattice are analyzed by means of a Delauney triangulation [12], which is constructed at each recorded time step. Each vortex in the bulk with fewer or more than six neighbors is identified with a defect in the lattice.

4. Computational Results

The results of the numerical computations for the standard configuration are summarized in Figs. 1 and 2.

4.1. No Transport Current

In the absence of a transport current, 230 vortices enter the sample to form a dilute vortex structure with an average lattice spacing $a_0 = 2.58\lambda$. The average magnetic induction in the sample is $B = 0.27$, considerably less than the applied field $H_0 = 0.8$. The lattice is static. Its structure remains defective; the major types of defects are isolated dislocations (pairs of defects—one with five, the other with seven neighbors) and finite segments of 30° boundaries (strings of three or more contiguous dislocations). The vortex region is separated from the free surfaces by a vortex-free region of width 2.1λ. The Meissner current flows entirely within these vortex-free regions.

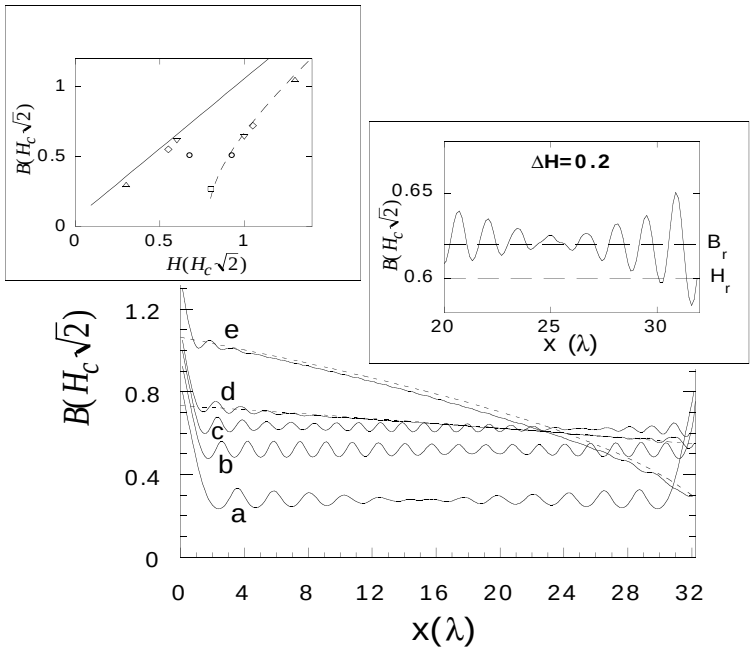

Fig. 1. Magnetic induction profiles (averaged over y) obtained from computations (solid lines) and theory (dashed lines); (a) no current, (b) weak current, (c) critical current, (d) intermediate current, (e) strong current. Left inset: Computed values of (H_l, B_l) and (H_r, B_r), with stability boundaries for the left (dashed line) and right (solid line) surface. Right inset: Magnetic induction profile near the right edge of the sample for critical current.

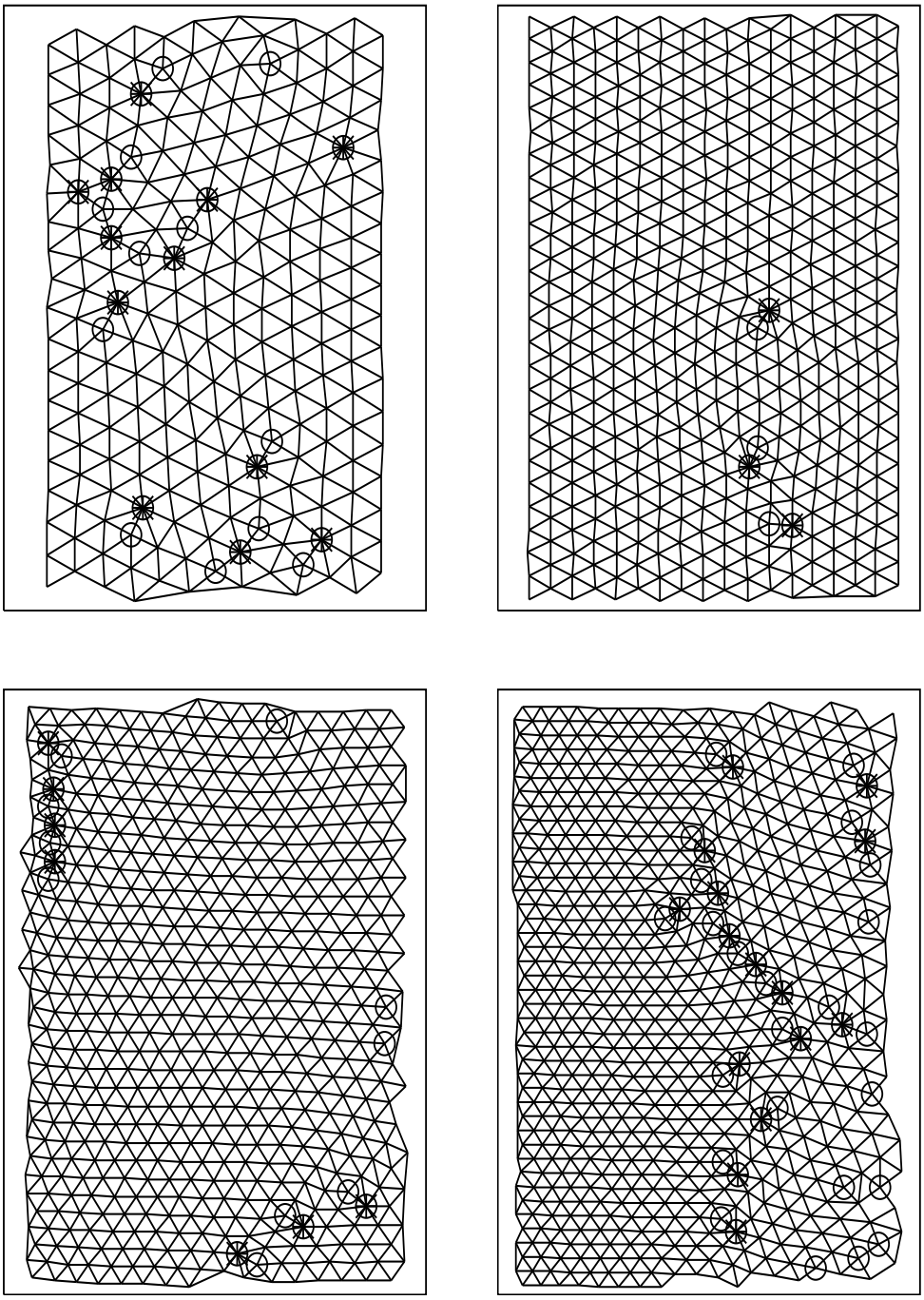

Fig. 2. Lattice structure in standard (32×48) sample (bulk only); $H_0 = 0.8$; lattice defects are marked. Top left: no current, top right: weak current, bottom left: intermediate current, and bottom right: strong current.

4.2. Weak Transport Current

A weak current ($\Delta H = 0.125$) almost doubles the average number of vortices to 459. The vortices form an almost ideal crystal structure, with $a_0 = 1.88\lambda$. The lattice is again static, but slightly displaced to the right edge, so the vortex-free region near the right surface is significantly narrower than near the left surface. The supercurrent density at the left edge of the sample is approximately equal to the BCS depairing-current density. The close-packed direction of the lattice is again aligned with the free surfaces. The remaining defects are the remnants of a misoriented grain in the center of the sample, whose origin goes back to the transient phase and which gradually heals during the recording period.

4.3. Intermediate Transport Current

So far, the Lorentz force has been too weak to overcome the surface barrier at the right edge. The vortices move only internally within the sample, and the lattice remains essentially static. This picture changes dramatically when we apply an intermediate transport current ($\Delta H = 0.250$). The surface barrier at the right edge is broken, and the lattice moves steadily in the positive x direction. At the left edge, vortices penetrate into the sample in a highly organized manner: A penetrating vortex triggers successive nucleations, which propagate along the surface of the sample in the direction of the current ("zipper" penetration). Vortices exit through the right surface, where the vortex-free region has disappeared completely. The average number of vortices in the sample increases to approximately 565; this number oscillates in time, but the amplitude of the oscillation is always less than 1%. The close-packed direction of the moving lattice is oriented along the direction of motion. A reorientation of a moving vortex lattice was observed in early experiments [13] and, more recently, in YBCO [14]. A mechanism for the reorientation in the presence of bulk pinning was proposed in the context of collective pinning theory in [15]. Our investigation indicates that the reorientation also can be caused by the free surfaces of the sample. Approximately one third of the transport current now flows in the interior the sample, supporting the steady motion of the lattice. The resulting small gradient in the vortex density leads to an expansion of the lattice as x increases.

4.4. Critical Transport Current

An estimate of the critical value of the current at which the vortex lattice begins to move can be obtained from the theories of Shmidt [16], Ternovskii and Shekhata [17], and Clem [18]. According to these authors, there are two critical curves in the (H, B) plane associated with any free surface of a type-II superconductor, $H = H_{\max}(B)$ and $H = H_{\min}(B)$. As long as $H > H_{\max}(B)$, vortices will break through the surface to enter the sample, thus increasing the magnetic induction just inside, until $H = H_{\max}(B)$. Similarly, as long as $H < H_{\min}(B)$, vortices will break through the surface to leave the sample, thus decreasing the magnetic induction just inside, until $H = H_{\min}(B)$. Approximate (dimensionless) expressions for $H_{\max}(B)$ and $H_{\min}(B)$ in the range $H_{c1} < B < H_{c2}$ are

$$H_{\max}(B) \approx \left(B^2 + H_p^2\right)^{1/2};\ H_{\min}(B) \approx B - B_0, \tag{4}$$

where $B_0 = (2\pi\sqrt{3})/(48\kappa)$ [17]. Usually, it is assumed that $H_p = H_c$.

The values of the applied and induced field near the left (subscript l) and right (subscript r) surfaces for the various currents are given in Table 1; the corresponding points are marked in Fig. 1 (left inset). A best fit of a curve $H = H_{\max}(B)$ through the data (H_l, B_l) for no current, weak current, and intermediate current yields $H_p \approx 0.78$; hence, our computations suggest that the penetration field in the Meissner state is $H_p \approx 1.1 H_c$. The dashed line in Fig. 1 (left inset) is the graph of $H_{\max}$ with $H_p = 0.78$. In Table 1, we have also listed the data (H_l, B_l) for the strong current (discussed below). The corresponding point in Fig. 1 (left inset) lies very close to the critical curve $H = H_{\max}(B)$—an indication that the expression for $H_{\max}(B)$ given in Eq. (4) remains a good approximation when the lattice moves faster. The solid line in Fig. 1 (left inset) is the graph of $H_{\min}$ for $\kappa = 4$.

The critical current $J_{\rm cr}$, at which the surface barrier at the right edge is first broken, can be estimated from Eq. (4),

$$J_{\rm cr} = 2(\Delta H)_{\rm cr} = \frac{H_p^2}{2H_0 + B_0} + B_0. \tag{5}$$

For $H_0 = 0.8$, we find $J_{\rm cr} \approx 0.42$. Computations with $\Delta H = 0.175, 0.195, 0.200$ show that vortices first break through the surface barrier at the right edge when $\Delta H = 0.200$. The average lattice spacing decreases from $a_0 \approx 1.84\lambda$ at $\Delta H = 0.175$ to $a_0 \approx 1.74\lambda$ at $\Delta H = 0.200$. The values of the applied and induced field near the free surfaces at the critical current are included in Table 1, and the corresponding points are marked in Fig. 1 (left inset). Also included in Fig. 1 (right inset) is a blow-up of the field profile for the critical current near the right edge of the sample. As predicted by Eq. (4), the value of B_r exceeds H_r by the small positive quantity B_0. This resolves the discrepancy about the sign of the correction in [17,18].

Table 1. Values of the applied and induced field near the left and right free surface

Current	H_l	B_l	H_r	B_r
no	0.800	0.27	0.800	0.27
weak	0.925	0.52	0.675	0.52
critical	1.000	0.640	0.600	0.615
intermediate	1.050	0.70	0.550	0.55
strong	1.300	1.04	0.300	0.30

The data (H_r, B_r) for no current and weak current lie below the graph—an indication that the surface barrier at the right edge has not been broken and the lattice is stationary. The data (H_r, B_r) for the intermediate and strong current lie on the line $B = H$. The surface barrier at the right edge of the sample has been broken, and the barrier force has no effect on the moving lattice.

4.5. Field Profiles

When the vortex lattice moves steadily across the sample, as for the intermediate current, the total current J splits into a surface contribution, J_s, and a bulk contribution, J_b. The self-field of the bulk transport current induces a gradient of the magnetic induction and, therefore, a gradient of the vortex density, and this gradient leads in turn to a deformation of the vortex lattice.

The field profile in the bulk can be found from the force balance equation for the overdamped steadily moving elastic vortex lattice, $\eta n \mathbf{v} = \nabla \cdot \overleftrightarrow{\boldsymbol{\sigma}}$. Here, η is the viscosity of the vortex lattice, $n = B/\Phi_0$ the vortex density, and $\mathbf{v}$ is the vortex velocity. The elastic stress tensor $\overleftrightarrow{\boldsymbol{\sigma}}$ is related to the strain tensor $\overleftrightarrow{\boldsymbol{\varepsilon}}$ via the matrix of elastic moduli C_{ij}, which vary nonlinearly with B. In the case of uniaxial compression in the x direction, the only nonzero component of the elastic strain tensor is ε_{xx}, so

$$\eta n v = C_{11}(B) \frac{\mathrm{d}\varepsilon_{xx}}{\mathrm{d}x}. \tag{6}$$

For a steadily moving vortex lattice, the flux nv is coordinate independent, so the expression in the left member is constant, equal to $\gamma/(8\pi)$, say. The elastic strain tensor relates the variation in the magnetic field to the local value of the field, $\delta B = \varepsilon_{xx} B$, so $\mathrm{d}\varepsilon_{xx}/\mathrm{d}x = -(1/B)(\mathrm{d}B/\mathrm{d}x)$. A good approximation for $C_{11}(B)$ in the range $H_{c1} < B \ll H_{c2}$ is $C_{11}(B) = (B^2/(4\pi))(1 - 1/(4\kappa B))$. Thus, B satisfies the differential equation

$$-2B \left(1 - \frac{1}{4\kappa B}\right) \frac{\mathrm{d}B}{\mathrm{d}x} = \gamma. \tag{7}$$

The equation can be integrated, for example, from the right edge, where $B = B_r$, into the bulk. The constant γ is then determined by the condition that $B = B_l$ at the left edge of the bulk. Identifying the width of the bulk with the width of the sample, d, we find the following expression for the magnetic field in the bulk:

$$B(x) = \frac{1}{4\kappa} + \left(\left(B_r - \frac{1}{4\kappa} \right)^2 + \gamma d \left(1 - \frac{x}{d} \right) \right)^{1/2}, \tag{8}$$

where $\gamma d = (B_l - B_r)(B_l + B_r - 1/(2\kappa))$. Substitution of the expressions $B_r = H_r = H_0 - \frac{1}{2}J$ and $B_l = H_l - J_s = H_0 + \frac{1}{2}J - J_s$ gives $B(x)$ in terms of H_0, J, and J_s. The dashed lines in Fig. 1 show the excellent agreement with the field profiles found in the computations. The agreement also demonstrates that the expression for $C_{11}(B)$ used in the derivation of Eq. (8) remains valid, even though the condition $B \ll H_{c2}$ is not really satisfied.

4.6. Strong Transport Current

We proceed to the case of a strong transport current, $\Delta H = 0.500$. The vortex lattice now moves very fast across the sample, and we observe several interesting new phenomena. The self-field of the transport current inside the sample induces a significant density gradient: The density near the left edge is approximately three times the density near the right edge (see Fig. 1). The lattice experiences a significant strain in the left part of the sample. Slightly beyond the center, it can no longer bear the strain, and plastic deformation occurs. A defect boundary ("fault line") appears, which consists of several aligned dislocations and finite segments of a 30° boundary. The fault line remains more or less stationary as the lattice moves across the sample. The critical strain $\varepsilon_{\rm pl}$, at which the lattice yields, can be estimated from the stretch in the horizontal bonds from the left edge to the fault line, $\varepsilon_{\rm pl} \approx 0.35$.

4.7. Plastic Deformation

The current at which the lattice first shows plastic deformation, $J_{\rm pl}$, can be estimated. As long as the strain near the right edge of the sample, $\varepsilon_{xx} = (B_l - B_r)/B_l$, is less than the plastic limit for uniaxial stretching, $\varepsilon_{\rm pl}$, the lattice is deformed elastically throughout the bulk. The fault line first appears at the right edge when $B_l - B_r = \varepsilon_{\rm pl} B_l$. With $B_l - B_r = J_{\rm pl} - J_s$ and $B_l = H_0 + \frac{1}{2} J_{\rm pl} - J_s$, we find

$$J_{\rm pl} = \frac{(1 - \varepsilon_{\rm pl}) J_s + \varepsilon_{\rm pl} H_0}{1 - \varepsilon_{\rm pl}/2}. \tag{9}$$

At stronger currents, plastic deformations appear at a finite distance $x_{\rm pl}$ from the left edge. This distance can be estimated from the relation $B_l - B(x_{\rm pl}) = \varepsilon_{\rm pl} B_l$. Using Eq. (8) for the field, we find

$$\frac{x_{\rm pl}}{d} = \varepsilon_{\rm pl} B_l \frac{(2 - \varepsilon_{\rm pl}) B_l - 1/(2\kappa)}{(B_l - B_r)(B_l + B_r - 1/(2\kappa))}. \tag{10}$$

Here, $B_l - B_r = J - J_s$ and $B_l = H_0 + \frac{1}{2} J - J_s$.

5. Defect Superstructure in Wider Samples

The development of a stationary defect superstructure in a moving vortex lattice is one of the main findings of our computations. Further computations have shown that, in a wider sample, this superstructure is even more developed. Figure 3 shows the lattice structure at the final recorded time step in a wide sample, whose cross section in the (x, y) plane measures 48×32. The value of the applied field at the right edge and the gradient of the applied field (that is, the transport current density) across the sample are the same as in the case of the strong current for the standard sample ($H_0 = 1.05$, $\Delta H = 0.75$). Several fault lines are necessary to support the large density differential across the sample. Figure 4 shows the magnetic induction profile as found in the computations and as theoretically predicted by Eq. (8).

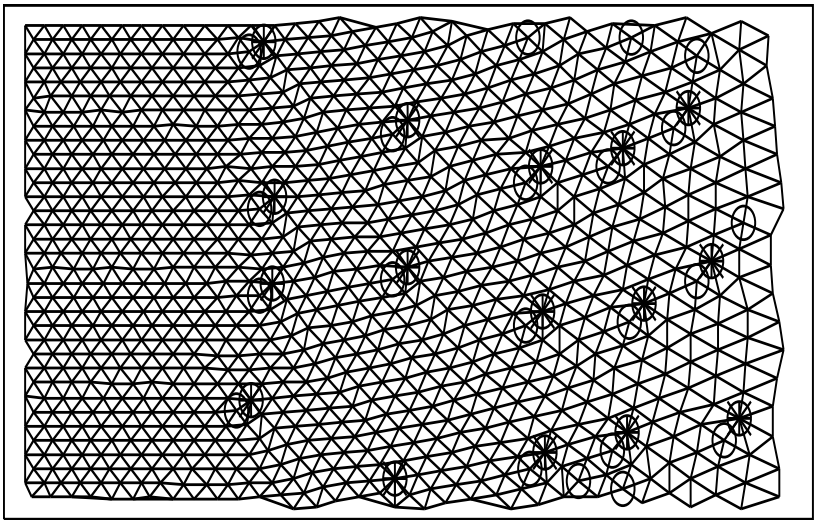

Fig. 3. Lattice structure in wide (48×32) sample (bulk only); $H_0 = 1.05$, $\Delta H = 0.75$; lattice defects are marked.

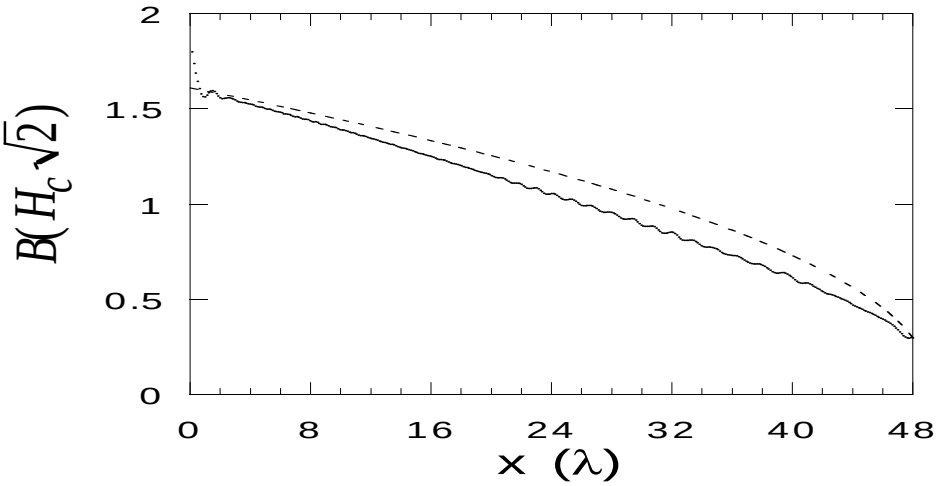

Fig. 4. Magnetic induction profile (averaged over y) in wide sample; $H_0 = 1.05$, $\Delta H = 0.75$; obtained from from computations (solid line) and theory (dashed line).

The defect superstructure is even more developed in the very wide sample shown in Fig. 5. The sample measures 72×32 in cross section. Again, the applied field is chosen so the transport current density is the same as in the case of the strong current for the standard sample ($H_0 = 1.425$ and $\Delta H = 1.125$). In both the wide and the very wide sample, the defect superstructure remains more or less stationary while the vortices stream across the sample. Note that the close-packed direction rotates each time a fault line is encountered.

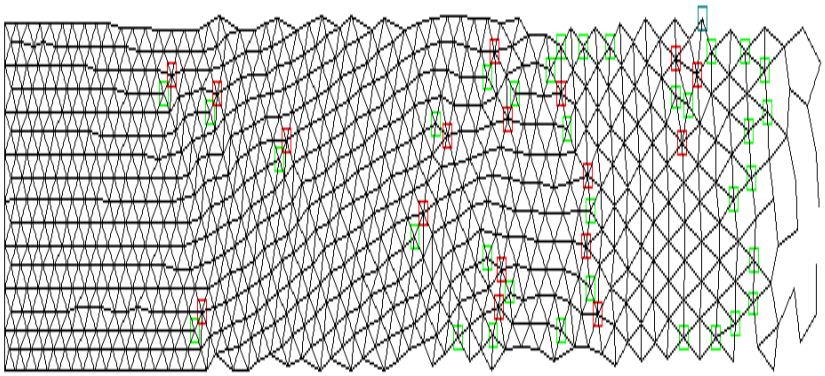

Fig. 5. Lattice structure in very wide (72×32) sample (bulk only); $H_0 = 1.425$, $\Delta H = 1.125$; lattice defects are marked.

6. Summary

Summarizing, we have shown a new mechanism for plastic motion of a driven vortex lattice in a clean superconductor. The mechanism involves the creation of a superstructure of lattice defects, which supports the gradient in the vortex density induced by the self-field of the current. Although the lattice moves across the sample, the defect superstructure remains static. We have also shown a dynamic reorientation of the lattice. When the current is weak, the lattice is essentially static, and its close-packed direction is aligned with the free surfaces. When the current exceeds a critical value, the lattice moves, and its close-packed direction is aligned with the direction of motion. Finally, we have shown a gradual healing of the lattice defects under the influence of a transport current.

References

[1] S. Bhattacharya and M. J. Higgins, Phys. Rev. Lett., **70**, 2617 (1993).

[2] W. K. Kwok et al., Phys. Rev. Lett., **73**, 2614 (1994).

[3] W. R. White, A. Kapitulnik, and M. R. Beasley, Phys. Rev. **B**, **50**, 6303 (1994) .

[4] S. N. Coppersmith, Phys. Rev. Lett., **65**, 1044 (1990).

[5] A. E. Koshelev and V. M. Vinokur, Phys. Rev. Lett., **73**, 3580 (1994).

[6] P. DeGennes, *Superconductivity in Metals and Alloys*. Benjamin, New York, 1966.

[7] A. Schmid, Phys. Kondens. Mater., **5**, 302 (1966); L. P. Gor'kov and G. M. Eliashberg, Zh. Eksp. Teor. Fiz., **54**, 612 (1968) [Sov. Phys. JETP **27**, 328 (1968)].

[8] U. Essmann and H. Träuble, Phys. Stat. Sol., **32**, 337 (1969).

[9] M. Marchevsky et al., Leiden University, preprint (1995).

[10] W. D. Gropp et al., J. Comp. Phys. (in press).

[11] M. Tinkham, *Introduction to Superconductivity*. McGraw-Hill, New York, 1975; Krieger Publ. Co., Malabar, Florida, 1995.

[12] F. F. Preparata and M. L. Shamos, *Computational Geometry: An Introduction*. Springer-Verlag, New York, 1985.

[13] A. T. Fiory, Phys. Rev. Lett., **27**, 501 (1971).

[14] J. M. Harris et al., Phys. Rev. Lett., **74**, 3685 (1995).

[15] A. Schmid and W. Hauger, J. Low Temp. Phys., **11**, 667 (1973).

[16] V. V. Shmidt, Zh. Eksp. Teor. Fiz. **61**, 398 (1971) [Sov. Phys. JETP **34**, 211 (1972)].

[17] F. F. Ternovskii and L. N. Shekhata, Zh. Eksp. Teor. Fiz. **62**, 2297 (1972) [Sov. Phys. JETP **35**, 1202 (1972)].

[18] J. R. Clem, in: *Proc. 13th Conf. on Low Temperature Physics* (LT 13), K. D. Timmerhaus, W. J. O'Sullivan, and E. F. Hammel, eds. Vol. 3, p. 102. Plenum, New York, 1974.